Available online at www.sciencedirect.com

ScienceDirect

Advances in Space Research 77 (2026) 923–938

ADVANCES IN SPACE RESEARCH (a COSPAR publication)

www.elsevier.com/locate/asr

GNSS-based real-time orbit determination and prediction for LEO-PNT ephemeris generation

Florian Kunzi *, Oliver Montenbruck, Francesca Perazzetti

German Aerospace Center/German Space Operations Center, Münchener Str. 20, Wessling 82234, Germany

Received 15 October 2025; received in revised form 17 November 2025; accepted 19 November 2025
Available online 24 November 2025

Abstract

Positioning, navigation and timing (PNT) with low Earth orbit (LEO) constellations requires precise knowledge of the navigation satellites' positions at the time of signal transmission. For conventional GNSS this is achieved by transmitting broadcast ephemerides via the navigation signals, allowing a user to predict the satellite's position at the required time. Similar approaches using perturbed Keplerian ephemeris models for LEO satellites have already been discussed in the literature. The ephemeris fitting process always requires a set of predicted satellite positions over the desired validity interval of the ephemeris. In a GNSS-augmented LEO-PNT architecture, the navigation satellites determine their position on-board in real-time using GNSS. Based on these orbit determination results, the satellites can autonomously predict their trajectory for fitting of on-board ephemeris parameters. This study assesses the real-time orbit prediction accuracy in LEO using real GNSS data from four satellites across different altitudes. With focus on navigation message generation for future LEO-PNT systems, predicted trajectory arcs of 20 min are assessed using GNSS broadcast ephemerides. At high atmospheric density near solar maximum the prediction error for altitudes around 500 km may well grow over 1 m, while for higher altitudes the error remains at low decimeter level. Furthermore, the effects of applying Galileo High Accuracy Service (HAS) corrections in a GPS/Galileo navigation filter are assessed for both orbit determination and orbit prediction. Additional considerations on the prediction performance are made, including the choice of atmospheric density model as well as navigation filter tuning and the consequences on real-time and predicted orbits. For LEO-PNT broadcast ephemeris generation, a representative LEO ephemeris model is adopted in the parameter fitting of the predicted trajectory arcs. The results demonstrate that the prediction error remains the dominant error source in an autonomous on-board ephemeris generation and exceeds the fitting error of adequate LEO-PNT ephemeris models. Depending on the LEO altitude, 1D line-of-sight user ranging errors of less than 8 cm over 20 min ephemeris validity intervals can be achieved using real-time orbit prediction.

Keywords: Orbit determination; Orbit prediction; LEO-PNT; Satellite Ephemeris; Galileo; HAS

1. Introduction

With the deployment of various mega-constellations, the number of low Earth orbit (LEO) satellites has been growing rapidly over the last years. While such constellations are mostly intended for telecommunications, the interest in positioning, timing and navigation (PNT) services from LEO as an enhancement or alternative to the conventional GNSS constellations in medium Earth orbit (MEO) has likewise increased. This includes efforts from industry such as XONA Pulsar (Reid et al., 2022), CentiSpace (Chen et al., 2023) or Geely (Van Uytsel et al., 2024), as well as agencies such as the European Space Agency (ESA; Le Priellec et al., 2025). Different LEO-PNT architectures have been proposed, such as GNSS-like concepts either independent from or slaved to GNSS (Eissfeller et al., 2024; Kunzi et al., 2023), hybrid concepts which fuse

* Corresponding author.
E-mail address: florian.kunzi@dlr.de (F. Kunzi).

https://doi.org/10.1016/j.asr.2025.11.082
0273-1177/

telecommunications and navigation services in one payload (Iannucci and Humphreys, 2022), or the usage of arbitrary signals of opportunity from LEO satellites for navigation (Kozhaya et al., 2025). Despite significant conceptual differences of the individual LEO-PNT architectures, knowledge of the instantaneous LEO satellite position is a common user requirement in all systems.

While, for scientific missions, it is often sufficient to obtain orbit products in post-processing on ground, the orbits of LEO-PNT satellites need to be determined in real-time to enable user positioning based on LEO-to-user ranging measurements. With the increased interest in new LEO-PNT systems, the problem of determining orbit and clock products of a PNT satellite as well as distributing this information to users has been discussed extensively. In view of large LEO-PNT constellations with hundreds to thousands of satellites, GNSS provides a feasible and cost-efficient solution for autonomous on-board orbit determination in real-time. GNSS-based orbit determination has been demonstrated to yield 3D root mean square (RMS) orbit errors in real-time at low decimeter level using observations from multiple constellations (Hauschild and Montenbruck, 2021; Montenbruck et al., 2022; Darugna et al., 2022).

In a LEO-PNT system, the onboard orbit estimate must be predicted ahead of time and approximated by a parameterized orbit model suitable for use in a broadcast navigation message. The required prediction arc and the length of the fit intervals for the orbit model are driven by the representative LEO visibility period for a ground based user, which ranges from 10–20 min for common LEO altitudes. Established broadcast ephemeris models such as those of the GPS legacy (LNAV) and civil (CNAV) navigation messages (GPS ICD, 2022) comprise between 15 and 17 orbit parameters, including six Keplerian elements as well as secular and harmonic perturbation coefficients. As the GNSS ephemeris is highly optimized for MEO, specific models for the LEO environment are required. A widely proposed approach is to enhance the GNSS ephemeris with additional rate terms, which account for perturbations specific to LEO such as atmospheric drag or the significantly increased influence of Earth's gravity. Meng et al. (2021b) propose a 22 parameter model, which achieves a fit error of 1.6 cm at 800 km altitude over 20 min trajectory arcs. Using a 21 parameter ephemeris model, Guo et al. (2022) demonstrate a fit error of less than 0.1 m for 20 min arcs at 500 km altitude. Other models use an enhanced version of the state vector representation used by the GLONASS broadcast ephemeris (Meng et al., 2021a) or geometrical approaches such as a b-spline representation (Dobbin and Axelrad, 2023), both as well with fit errors of less than 0.1 m. De Oliveira Salgueiro et al. (2024) propose a combination of GNSS or purely Keplerian models with Chebyshev polynomials for a potential LEO-PNT navigation message and assess the achievable performance over multiple fit intervals for four spacecraft at different altitudes. Overall, existing literature has demonstrated that it is possible to fit LEO-specific ephemeris parameters to well below a decimeter error with respect to the underlying set of satellite position vectors.

While onboard orbit determination and orbit parameter fitting for LEO-PNT systems have been duly covered in the literature, only limited attention has been paid to the achievable performance of autonomous on-board orbit prediction. Building on a representative real-time orbit determination process for LEO-PNT satellites (Kunzi et al., 2023), the achievable performance of short-term orbit prediction and ephemeris fitting is assessed based on a set of reference missions at different orbital altitudes. For a worst-case consideration, a high-drag regime is selected. First, the study's general methodology including the spacecraft and datasets used for the assessment is presented. This is followed by a description of the real-time orbit determination algorithms and the performance evaluation process. Thereafter, the results are presented and discussed, leading to several suggestions for improving real-time prediction performance.

2. Spacecraft and datasets

This study evaluates the performance of GNSS-based real-time orbit determination, prediction, and ephemeris model fitting for LEO satellites using real GNSS measurements of four different missions as listed in Table 1. With Swarm-C at 460 km (Friis-Christensen et al., 2008), Sentinel-2C and Sentinel-3A at approximately 800 km (Fernández et al., 2016), as well as Sentinel-6A at 1336 km (Donlon et al., 2021), the data sets cover a representative range of LEO altitudes to assess altitude-dependent effects on both orbit determination and prediction. Furthermore, the different satellites allow to evaluate the performance with GPS-only (Swarm-C, Sentinel-3A, Sentinel-6A) and Galileo/GPS (Sentinel-2C, Sentinel-6A) measurements, respectively. The two GNSSs differ notably in the signal-in-space range error (SISRE) of their navigation messages (Montenbruck et al., 2018). This is reflected in roughly a factor of two improvement for the resulting real-time navigation accuracy and is also found to benefit the resulting orbit prediction performance. In the case of Sentinel-6, two independent GNSS receivers are flown on the same satellite. While the TriG receiver (Young, 2017) supports only GPS tracking, both Galileo and GPS observations are provided by the PODRIX receiver (Peter et al., 2022), albeit with a lower number of tracking channels for the individual constellations. Within this study, we make use of both receivers to individually assess the performance of GPS-only and combined GPS/Galileo real-time navigation and prediction at the given orbit altitude.

As the evaluation period, 14 consecutive days from November 28 to December 11, 2024, corresponding to day of year (DOY) 333 to 346, were selected. With the current solar cycle reaching its maximum in 2025, the

Table 1
Spacecraft used for the orbit determination and prediction assessment. GNSS signals are identified by their RINEX (Gini, 2024) observation codes.

	Swarm-C (SWC)	Sentinel-2C (S2C)	Sentinel-3A (S3A)	Sentinel-6A (S6A)
Orbit altitude [km]	460	786	810	1336
Inclination [deg]	87.2	98.6	98.6	66
Orbital period [min]	94	100	101	112
Mass [kg]	384	1142	1101	1180
GNSS Constellations	GPS	Galileo/GPS	GPS	Galileo/GPS (PODRIX receiver) GPS (TriG receiver)
GPS Signals	1W, 2W, 1C	1W, 2W, 1C, 2L	1W, 2W, 1C	1W, 2W, 1C, 2L (PODRIX) 1W, 2W, 1C (TriG)
Galileo Signals	–	1C, 5Q	–	1C, 5Q (PODRIX)

period exhibits a high solar activity with maximum $F_{10.7}$ and K_p indices of 220 and 4.7, respectively, impacting the real-time orbit determination of the analyzed datasets. A higher solar activity increases the atmosphere's temperature more than usual during daytime, causing it to rise to higher altitudes, which consequently increases the atmospheric density in LEO compared to medium solar activity. These thermal variations render the modeling of the atmospheric density in real-time significantly more complex and are particularly challenging at the lower range (400–600 km) of LEO altitudes. Note that during the evaluation period, orbit maneuvers were performed by Sentinel-2C (1 maneuver) and Swarm-C (2 maneuvers). During the maneuver phase, the orbit determination was continued but no orbit prediction was performed for these spacecraft, as maneuver handling would require additional considerations in the prediction framework which are out of scope for this study.

The reference orbits for the four different spacecraft are obtained from precise orbit determinations (PODs) in ground-based post-processing. For the Sentinel satellites, combined orbit products of the Copernicus POD (CPOD) service are used (Fernández et al., 2024), while the Precise Science Orbits of TU Delft (van den IJssel et al., 2015) serve as reference for Swarm-C.

3. Methodology

3.1. Reduced dynamic orbit model

The core of both the orbit determination and prediction algorithms presented in the following subsections is a reduced dynamic orbit model (Wu et al., 1991). It describes the satellite's trajectory based on a combination of modeled and empirical accelerations. This study employs a formulation in the Geocentric Celestial Reference Frame (GCRF) for the equation of motion and consequently also uses the GCRF for the estimation of the satellite's position and velocity. Compared to a formulation in the rotating Earth-fixed International Terrestrial Reference Frame (ITRF) as suggested by Montenbruck and Ramos-Bosch (2008), the inertial formulation requires an increased effort for the GCRF-to-ITRF transformation in the measurement model, but avoids subtle errors in the approximate expressions for Coriolis and centrifugal forces. Nevertheless, transformations between GCRF and ITRF still need to be performed to model specific accelerations, e.g. Earth's gravity, which is typically evaluated in an Earth-fixed frame. This transformation process requires knowledge of the Earth rotation parameters (EOP). While in the past, the EOP had to be obtained from sources such as the International Earth Rotation Service (IERS) and frequently uploaded to the spacecraft, EOPs can nowadays be retrieved onboard from the navigation messages of several GNSSs including GPS and BeiDou. For this study, the EOP transmitted in the CNAV navigation message of the GPS L2C signal are employed (GPS ICD, 2022). While broadcast EOP tend to have a lower accuracy than those observed by the IERS, their quality was previously shown to be adequate for use in spacecraft navigation (Steigenberger et al., 2022).

The reduced dynamic orbit model describes the total acceleration $\boldsymbol{a}_{\text{sat}}$ acting on the satellite as the sum of different accelerations caused by various orbital perturbations. The force model employed for this study is presented in Table 2. In view of potential limitations in computational performance of on-board processors as well as real-time requirements, perturbations with a comparably small impact, such as ocean tides or relativity, are omitted. Thus, the accelerations acting on the satellite with position $\boldsymbol{r}$ and velocity $\boldsymbol{v}$ at epoch t_i are described as

$$\begin{aligned}&\boldsymbol{a}(\boldsymbol{r},\boldsymbol{v},C_D,C_R,t_i)=\\&\boldsymbol{a}_{\text{grav(Earth)}}(\boldsymbol{r})+\boldsymbol{a}_{k_2}(\boldsymbol{r},t_i)\\&+\boldsymbol{a}_{\text{grav(Sun)}}(\boldsymbol{r},t_i)+\boldsymbol{a}_{\text{grav(Moon)}}(\boldsymbol{r},t_i)\\&+\boldsymbol{a}_{\text{SRP}}(\boldsymbol{r},t_i,C_R)+\boldsymbol{a}_{\text{drag}}(\boldsymbol{r},\boldsymbol{v},t_i,C_D)\\&+\boldsymbol{a}_{\text{emp},i}(t_i),\end{aligned}\tag{1}$$

where the different vectors $\boldsymbol{a}$ describe the accelerations caused by Earth's gravity, k_2 solid Earth tides, atmospheric drag, solar radiation pressure (SRP), as well as third-body gravitation from the Sun and Moon, respectively. The empirical accelerations $\boldsymbol{a}_{\text{emp}}$ are estimated in the real-time navigation filter and compensate for residual accelerations not covered by the trajectory model. The relative contributions of several individual accelerations, especially

Table 2
Reduced dynamic orbit model used by the navigation filter and the orbit prediction algorithm.

Category	Item	Description
Force Model		
	Earth gravity	GOCO03S (Tapley et al., 2004) up to order and degree 70, rate terms $\dot{C}_{20}, \dot{C}_{21}, \dot{S}_{21}$
	Solid Earth tides	k_2 tides (Rizos and Stolz, 1985)
	Third-body gravity	Sun and Moon as point-masses with truncated series of luni-solar coordinates (Montenbruck and Gill, 2000)
	Atmospheric drag	Cannonball model; Atmospheric density obtained from Harris-Priester model for medium solar flux (Harris and Priester, 1962; Montenbruck and Gill, 2000)
	Solar radiation pressure	Cannonball model; cylindrical Earth shadow model (Montenbruck and Gill, 2000)
	Earth radiation pressure	Constant acceleration in radial direction
	Ocean tides	neglected
	Relativity	neglected
Estimated parameters		
	Empirical accelerations	Vector in radial, along- and cross-track (RAC) axes
	Radiation pressure coefficient	Scalar value w.r.t. constant cross-sectional area A (Eq. (2))
	Drag coefficient	Scalar value w.r.t. constant cross-sectional area A (Eq. (3))
General properties		
	Reference frame	Geocentric Celestial Reference Frame (GCRF)
	Earth orientation	GPS CNAV Earth Orientation Parameters (EOP; GPS ICD, 2022)
	ITRF transformation	IERS 1996 Conventions (McCarthy, 1996)
	Numerical integration	5th-order Dormand-Prince with 4th-order interpolant, fixed step size (Dormand and Prince, 1980)

atmospheric drag but also Earth's gravity, strongly depend on altitude within LEO. While the force model can be used anywhere in LEO, orbital perturbations such as gravitational forces and atmospheric drag become more complex at lower altitudes. Consequently, a degraded orbit determination and prediction performance is to be expected at lower altitudes.

Earth's gravity constitutes the predominant acceleration acting on a satellite in LEO. For precise orbit determination, it is important to consider the perturbations caused by the non-uniformity of the geopotential. For this study, the static GOCO03S gravity model (Tapley et al., 2004) is utilized. While more sophisticated, time-varying gravity models are available, such models appear less suitable for real-time on-board processing with limited computational resources. GOCO03S provides tesseral and sectorial geopotential coefficients, which are used to evaluate Earth's gravity at any position using a spherical harmonics expansion. For higher orbits like Sentinel-6A, considering geopotential coefficients up to order and degree 50 is sufficient for real-time orbit determination (Montenbruck et al., 2022). However, low orbits like Swarm-C at around 460 km altitude benefit from an extended gravity model (Hauschild and Montenbruck, 2021). Thus, the force model utilized in this study uses geopotential coefficients up to order and degree 70. Contributions of the solid Earth tides are modeled using a simplified k_2 tide model (Rizos and Stolz, 1985). Furthermore, the gravitational forces of Sun and Moon need to be considered in the force model. Unlike for Earth's gravity, it is sufficient to consider the two bodies as point masses. The positions of both Sun and Moon are approximated with a sufficient accuracy using truncated harmonic series (Montenbruck and Gill, 2000).

Atmospheric drag as well as SRP constitute the main non-gravitational forces acting on a LEO satellite. In the basic model adopted here, the acceleration caused by SRP is described as

$$\boldsymbol{a}_{\mathrm{SRP}} = C_R \cdot \frac{A}{m_{\mathrm{sat}}} \cdot \frac{\boldsymbol{d}}{||\boldsymbol{d}||^3} \cdot \mathrm{AU}^2 \cdot P_0 \tag{2}$$

where m_{sat} and A are the satellite's mass and cross-section, $\boldsymbol{d}$ denotes the Sun-to-satellite vector, AU is the astronomical unit, and $P_0 = 1367\mathrm{W/m}^2$ the solar flux at a distance of 1 AU. The acceleration caused by atmospheric drag is described as

$$\boldsymbol{a}_{\mathrm{drag}} = -\frac{1}{2} \cdot C_D \cdot \frac{A}{m_{\mathrm{sat}}} \cdot \rho \cdot \boldsymbol{v}_{\mathrm{sat,rel}} \cdot ||\boldsymbol{v}_{\mathrm{sat,rel}}||, \tag{3}$$

where $\boldsymbol{v}_{\mathrm{sat,rel}}$ denotes the satellite's velocity relative to the Earth's atmosphere and ρ is the atmospheric density. For this study, ρ is obtained from the Harris Priester model (Harris and Priester, 1962) or, if explicitly stated, from the Jacchia-71/Gill model (Jacchia, 1971; Montenbruck and Gill, 2000). Compared to more detailed atmospheric composition models such as NRLMSIS-00, the Jacchia-71/Gill model offers a notably reduced computationally complexity, while properly capturing the influence of solar-geophysical parameters on the total atmospheric density. As such, it provides a viable alternative to more sophisticated density models and a good compromise between accuracy and computational complexity for use in real-time applications. Furthermore, to avoid the usage of complex spacecraft macro-models in the real-time navigation filter, a cannonball model assuming a constant cross-sectional area A is adapted for both atmospheric drag and SRP. The coefficients C_D and C_R thus act as scale-

factors and are estimated epoch-wise in the navigation filter as shown in Eq. (6). However, a significant uncertainty in the atmospheric drag model remains the time-varying atmospheric density, which is strongly influenced by space weather and thus poses a major challenge for accurate drag modeling in real-time.

The reduced dynamic orbit model enables propagation of the satellite state vector

$$\boldsymbol{y} = \begin{pmatrix} \boldsymbol{r} \\ \boldsymbol{v} \end{pmatrix}, \tag{4}$$

where $\boldsymbol{r}$ and $\boldsymbol{v}$ are the satellite's position and velocity, respectively. Its change in time is described by the 1st-order differential equation

$$\dot{\boldsymbol{y}} = \begin{pmatrix} \dot{\boldsymbol{r}} \\ \dot{\boldsymbol{v}} \end{pmatrix} = \begin{pmatrix} \boldsymbol{v} \\ \boldsymbol{a} \end{pmatrix}, \tag{5}$$

where $\boldsymbol{a}$ is obtained from Eq. (1) and is a function of the instantaneous position and velocity as well as the empirical accelerations and drag/SRP scale factors estimated by the real-time navigation filter in the latest update step. Using numerical integration, the satellite state vector is propagated between consecutive filter update steps. This process enables a precise prediction of the satellite's trajectory based solely on the information obtained from the navigation filter. Among the various available numerical integration methods, the 5th-order Dormand-Prince integrator (DP5; Dormand and Prince, 1980) has proven to be well suited for real-time on-board orbit prediction (Montenbruck and Gill, 2001). DP5 can be combined with a 4th order interpolant, which builds on the intermediate values of the state vectors and does not require additional acceleration computations (Hairer et al., 1987). Based on this interpolant, the state vector can be evaluated at any point in time within the integration step with an accuracy compatible with the final integration state itself. This is especially useful for on-board applications which require the satellite's position and velocity at a higher rate than the update rate of the navigation filter. In addition to the numerical integration of the satellite state vector, the corresponding variational equations are integrated in a separate process to obtain the respective components of the navigation filter's state transition matrix. These include the gravity field gradient as well as partials for SRP and drag as well as for the empirical accelerations (Montenbruck and Gill, 2000).

3.2. Real-time navigation filter

The real-time navigation system adopted for this study consists of an extended Kalman filter (EKF), which fuses GNSS measurements with a reduced dynamic orbit model. The system has earlier been validated with GPS-only as well as multi-GNSS measurements (Montenbruck and Ramos-Bosch, 2008; Hauschild and Montenbruck, 2021) and could demonstrate a sub-decimeter level accuracy on the Sentinel-6A spacecraft using only broadcast ephemerides (Montenbruck et al., 2022). Additional performance improvements of around 10 % could be achieved when using GPS/Galileo measurements (Hauschild et al., 2022) in combination with the Galileo High Accuracy Service (HAS), which offers orbit and clock corrections as well as observable-specific code biases for Galileo and GPS broadcast ephemerides via the C/NAV navigation message of the Galileo E6-B signal.

The state vector of the navigation filter is defined as

$$\boldsymbol{x} = [\boldsymbol{r}; \boldsymbol{v}; \boldsymbol{a}_{\mathrm{emp}}; C_D; C_R; c\mathit{dt}_{\mathrm{rcv(X)}}; c\boldsymbol{dt}_{\mathrm{ISB}}; \boldsymbol{N}_{\mathrm{amb}}], \tag{6}$$

where $\boldsymbol{r}$ and $\boldsymbol{r}$ denote the position and velocity of the satellite's center of mass (COM) in the GCRF. The receiver clock offset $c\mathit{dt}_{\mathrm{rcv(X)}}$ with respect to the system time of GNSS X, here either Galileo system time (GST) or GPS time (GPST), is expressed in units of distance. In case of multi-GNSS measurements, an inter-system bias $\mathrm{ISB}_{\mathrm{Y-X}}$ for each additional GNSS Y is also included as part of the vector $c\boldsymbol{dt}_{\mathrm{ISB}}$. The empirical accelerations $\boldsymbol{a}_{\mathrm{emp}}$ in radial, along-track and cross-track direction are used to consider any residual accelerations that are not explicitly included in the deterministic force model. $\boldsymbol{a}_{\mathrm{emp}}$ is treated as an exponentially correlated random variable (ECRV) with configurable time constant and steady state covariance (Schutz et al., 2004). It is estimated as part of the filter state to provide a best fit of the observations under the constraints of the predefined stochastic properties. C_D and C_R denote the drag and radiation pressure coefficients, respectively, assuming a common and constant cross-sectional area A as explained in Section 3.1. Finally, the navigation filter estimates the carrier phase float ambiguities in the vector $\boldsymbol{N}_{\mathrm{amb}}$ in range units. Within the filter, the ambiguities are treated as stochastic parameters, which are propagated as constant values in the time update step, while their covariance is incremented with white process noise. In this way, signal-in-space range errors (SISRE) related to the use of broadcast ephemerides in the measurement model can be partly compensated in the filter. Compared to use of dedicated SISRE states (Gunning et al., 2019; Carlin et al., 2021), the use of "pseudo-ambiguities" (Montenbruck and Ramos-Bosch, 2008; Wang et al., 2015) lumping the actual phase ambiguities and the SISRE contribution in a common state parameter enable a notably leaner filter design while offering a similar performance in practice.

The estimated receiver clock offset $c\mathit{dt}_{\mathrm{rcv(X)}}$ describes the difference between the local receiver timescale and the timescale realized by the broadcast ephemerides of GNSS X. The latter timescale itself is an approximation of the actual GNSS time scale, which is realized by the respective ground segment. As each GNSS holds its own broadcast ephemeris time scale, a dedicated GNSS(Y)-to-GNSS(X) system time offset ($\mathrm{GGTO}_{\mathrm{Y-X}}$) has to be considered for each additional GNSS. In addition to the GGTO, the $\mathrm{ISB}_{\mathrm{Y-X}}$ also incorporates receiver-specific biases, which occur in the signal tracking between the two GNSSs. Consequently, the

receiver clock offset of GNSS Y can be expressed using the estimated clock offset of GNSS X and the respective ISB

$$cdt_{\mathrm{rcv(Y)}} = cdt_{\mathrm{rcv(X)}} + \mathrm{ISB}_{\mathrm{Y-X}}, \tag{7}$$

which is required for a correct modeling of the measurements as described in the next subsection. In the case of the Sentinel-2C and −6A spacecraft providing both Galileo and GPS measurements, this study always uses Galileo as the primary GNSS X. Thus, for these cases the filter estimates both $cdt_{\mathrm{rcv(GAL)}}$ and $\mathrm{ISB}_{\mathrm{GPS-GAL}}$, which consequently also allows to determine $cdt_{\mathrm{rcv(GPS)}}$ required for the measurement equations discussed in Section 3.2.2.

The update rate of the navigation filter is naturally limited by the sampling interval of the GNSS observations, which ranges from 1–10 s for the considered space missions. However, no significant performance differences between update intervals of 10 s and 30 s have been observed in this study, and even longer intervals of 60 s were successfully used for, e.g., Sentinel-6A in Montenbruck et al. (2022). However, at such an update rate, the orbit determination for satellites at lower altitudes, here Swarm-C, tends to show a decrease in performance. Thus, for this study, a 30 s measurement rate is used for all spacecraft.

3.2.1. Time update

During the filter's time update, the estimated state vector $\boldsymbol{x}$ is propagated from the last filter epoch $i-1$ to the current epoch i using appropriate propagation models for each state variable. The satellite's position and velocity are propagated with the trajectory model previously described in Section 3.1. In accord with the ECRV formulation, an exponential decay model

$$\boldsymbol{a}_{\mathrm{emp,i}} = \boldsymbol{a}_{\mathrm{emp,i-1}} \cdot m_i \quad \text{with} \quad m_i = e^{-(t_i - t_{i-1})/\tau} \tag{8}$$

is applied for the empirical accelerations, where τ is the exponential time constant after which the empirical accelerations are reduced to $1/e$. The remaining states including clock offset $cdt_{\mathrm{rcv,X}}$, potential inter-system biases $\mathrm{ISB}_{\mathrm{Y-X}}$, drag and solar radiation coefficients C_D and C_R as well as the float ambiguities N_{amb} are all propagated as constant values with white process noise.

As the final for the time update, the process noise matrix $\boldsymbol{Q}$ needs to be evaluated. In the case of the satellites' position-velocity state, no explicit process noise is considered, since the stochastic properties of the state propagation is already fully captured by the process noise of the empirical accelerations and the drag/SRP scale factors. While a white noise model with a constant process noise variance per unit time is applied for the drag and SRP coefficients (see Table 3), the process noise covariance of the empirical accelerations is given by

$$\boldsymbol{Q}_{\mathrm{aemp}} = \mathrm{diag}(\boldsymbol{\sigma}^2_{\mathrm{aemp}}) \cdot (1 - m_i)^2. \tag{9}$$

Here, the vector $\boldsymbol{\sigma}_{\mathrm{aemp}}$ contains the steady state process noise variances for the radial (R), along-track (A) and cross-track components (C), and m_i denotes the exponential decay factor defined in Eq. (8). For the receiver clock offset, a white noise model is again adopted with a process noise variance reflecting the stability of the receiver's reference oscillator over the update interval of the Kalman filter. The process noise for the ISB vector, on the other hand, is defined by the stability of broadcast time scales between the respective GNSSs, with variations at the millimeter-level per second. Finally, white process noise with a variance at the level of a few tenth of a mm^2/s is applied for the pseudo-ambiguities to account for the gradual variation of the broadcast ephemeris errors.

Table 3
Representative process noise values for the estimated force model parameters of the four different spacecraft.

Variable	SWC	S2C	S3A	S6A
$\sigma_{\mathrm{aemp,R}}$ [nm/s^2]	5.0	1.5	1.5	1.0
$\sigma_{\mathrm{aemp,A}}$ [nm/s^2]	80.0	10.0	4.0	3.5
$\sigma_{\mathrm{aemp,C}}$ [nm/s^2]	30.0	20.0	20.0	15.0
$\tau[s]$	600	600	600	600
C_D [–]	0.5	0.5	0.5	0.1
C_R [–]	0.1	0.1	0.1	0.1

3.2.2. Measurement update

Within the measurement update, the navigation filter processes the ionosphere-free combinations of dual-frequency GNSS pseudoranges and carrier phases. To ensure a consistent filter performance and to increase the navigation system's robustness, it is mandatory to identify measurement outliers in advance. Thus, a data screening of all available measurements is carried out. In a first step, observable residuals are calculated based on the predicted satellite state position and clock offset. Due to the assumption of a constant clock offset during time update, a clock correction term ∂cdt is then calculated based on the residuals using a least squares adjustment. The uncertainties of the now corrected residuals are obtained from the predicted covariance of the LEO satellite's position with respect to the corresponding GNSS satellite's LOS vector. Finally, the corrected residuals are scaled by their respective uncertainty and are compared against a threshold using a χ^2-test to identify and reject any measurement which does not meet the test condition. Note that as the here evaluated satellites are all equipped with geodetic-grade GNSS antennas and thus provide high-quality GNSS measurements, only a very small amount of measurements is rejected by the data screening process.

The measurement model for the pseudorange ρ_k for the k-th GNSS satellite is defined as

$$\rho_k = ||\boldsymbol{r}_{\mathrm{GNSS},k} - \boldsymbol{r}_{\mathrm{sat(APC)}}|| + cdt_{\mathrm{GNSS},k} - cdt_{\mathrm{rcv(GNSS)}} + B^{f_1,f_2}_{\mathrm{code},k} \tag{10}$$

where $\boldsymbol{r}_{\mathrm{GNSS},k}$ is the position of the antenna phase center (APC) of the GNSS satellite and $\boldsymbol{r}_{\mathrm{sat(APC)}}$ is the APC position of the LEO spacecraft. The modeled measure-

ments are corrected by the respective GNSS satellite clock offset cdt_{GNSS} as well as the receiver clock offset $cdt_{\mathrm{rcv(GNSS)}}$ referring to the respective GNSS.

Furthermore, the pseudorange modeling requires consideration of satellite code biases $B_{\mathrm{code},k}$. The different ranging code signals transmitted by GNSS satellites have distinct biases with respect to each other, caused by internal hardware delays on-board of the satellites (Montenbruck and Hauschild, 2013). For this reason, clock offsets in a GNSS navigation message refer to a conventional clock reference signal or signal combination. In addition, the various navigation messages provide biases for other transmitted signal with respect to this reference. For GPS, clock offsets refer to the L1/L2 P(Y) dual-frequency combination, while timing group delays (TGD) as well as inter-signal corrections (ISCs) in the LNAV and/or CNAV message support the processing of L1 C/A, L2C, and L5 signals. For Galileo, clock offsets in the F/NAV message are referenced to the E1/E5a signal combination, while I/NAV clock offsets refer to E1/E5b. For single-frequency processing or other dual-frequency combinations, different types of broadcast group delays (BGDs) are provided in the Galileo navigation messages. In the case of the PODRIX receivers of Sentinel-2C and Sentinel-6A, tracking of the GPS IIR-M and later satellites is limited to the civil L1 C/A and L2C signals. Consequently, those signals require the consideration of the TGD and the respective ISCs obtained from the GPS CNAV message in the measurement model (Tetewsky et al., 2009).

Similar to Eq. (10), the carrier phase φ_k for satellite k is described by

$$\varphi_k = ||\boldsymbol{r}_{\mathrm{GNSS},k} - \boldsymbol{r}_{\mathrm{sat(APC)}}|| + cdt_{\mathrm{GNSS},k} - cdt_{\mathrm{rcv(GNSS)}} + N_{\mathrm{amb},k}, \tag{11}$$

where, in contrast to the pseudorange model's code bias, the respective ambiguity term $N_{\mathrm{amb},i}$ is incorporated. In the present filter design, the float-valued (pseudo-) ambiguities are estimated as part of the filter state and aggregate the actual carrier phase ambiguity as well as signal-in-space ranging errors.

3.3. Real-time orbit prediction framework

This study analyzes the performance of short-term orbit prediction based on the results of the GNSS-based real-time navigation filter described in Section 3.2. Both the orbit determination and the prediction process are performed in a simulation environment representative of an application on-board of a LEO satellite. The time update step of the navigation filter and the real-time prediction framework use the same orbit model, but with different in- and outputs. Fig. 1 illustrates both processes for a measurement epoch t_i. In the orbit determination depicted in the top row, the time update step of the navigation filter propagates the filter state from the previous measurement epoch t_{i-1} to the current epoch t_i. Therefore, the numerical integrator is initialized with the satellite state vector $\boldsymbol{y}_{i-1}$ and the acceleration $\boldsymbol{a}_{i-1}$ as well as the force model parameters $C_{D,i-1}$, $C_{R,i-1}$, and $a_{\mathrm{emp},i-1}$ estimated by the filter during the past measurement update at epoch t_{i-1}. After the navigation filter has corrected its state in the current measurement update using GNSS observations at t_i, the a posteriori state vector $\boldsymbol{x}_i$ is utilized to perform a prediction of the satellite's trajectory as shown in the bottom row of Fig. 1. The prediction is carried out over a total duration ΔT using the same reduced dynamic orbit model as the navigation filter. To obtain an adequate number of intermediate sample points for fitting of the LEO-PNT ephemeris model, the integration is split into steps with a fixed step size $\Delta t = 30s$.

For each step, the integrator is re-initialized with the predicted state vector obtained from the previous step, requiring a total of $\Delta T/\Delta t$ integration steps for the overall trajectory arc. By storing the resulting DP5 interpolants after each step, the predicted position can be retrieved at any point in time within the overall prediction interval ΔT.

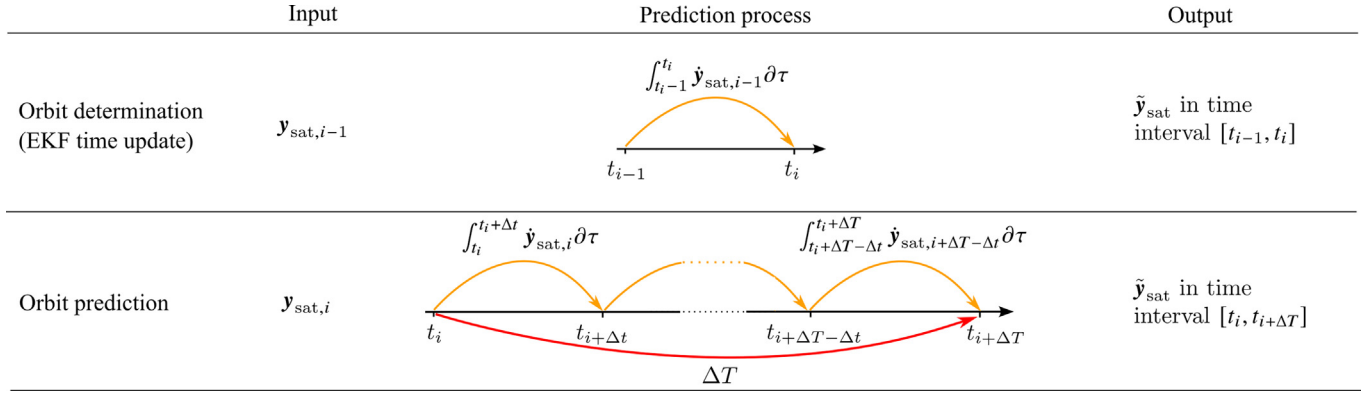

Fig. 1. Reduced dynamic orbit model applied to time update of the real-time navigation filter (top) and for the short-term orbit prediction (bottom) at measurement epoch t_i yield knowledge of the satellite's trajectory over different time intervals. Δt and ΔT denote the lengths of individual propagation steps and the overall prediction arc.

Fig. 2 depicts the analysis concept for assessing the performance of the real-time trajectory prediction process. Compared to the POD reference indicated by a black arrow, the real-time navigation filter obtains a slightly different estimate of the satellite trajectory, which is depicted as a blue line. At each GNSS measurement epoch t_n, the a posteriori satellite state vector $\hat{\boldsymbol{x}}_{\mathrm{sat,n}}$ as obtained by the navigation filter represents the best estimate of the satellite's position and velocity available in real-time on-board of the satellite. The trajectory is then predicted step-wise using the adopted orbit model over the time interval ΔT, depicted as red lines. These predicted trajectory arcs naturally deviate from both the estimated and the reference orbit due to estimation and measurement errors in the initial state vector as well as imperfect modeling of the forces acting on the satellite.

The force model parameters estimated in the real-time navigation filter, namely $\boldsymbol{a}_{\mathrm{emp}}, C_D$ and C_R, require careful consideration when being introduced in the prediction process. While for the orbit determination, the parameters are adjusted by the filter at each epoch based on the GNSS measurements, the prediction process has only knowledge about the parameter's zero-of-age values. Propagation of these parameters over the prediction interval ΔT becomes difficult due to the lack of proper prediction models. As the majority of the residual perturbations modeled by the empirical accelerations exhibit once-per-revolution frequencies (Colombo, 1989), $\boldsymbol{a}_{\mathrm{emp}}$ can significantly change over the prediction interval ΔT. Thus, a feasible approach is to assume an exponential decay as used in the filter's time update (see Eq. (8)). This ensures, on the one hand, consideration of the latest estimate of the empirical accelerations in the beginning of the prediction interval. On the other hand, their impact is continuously reduced over time to avoid introduction of erroneous residual accelerations in the force model, which would likely lead to a cumulative degradation in prediction accuracy. For the drag and SRP coefficients, however, no appropriate model is available to propagate the parameters throughout ΔT. Therefore, the only viable solution is to keep both coefficients constant w.r.t. the zero-of-age values provided by the real-time navigation filter. This renders the prediction process error-prone over longer periods of time, though, as the accuracy of the modeled drag and SRP forces likely degrades with increasing prediction time.

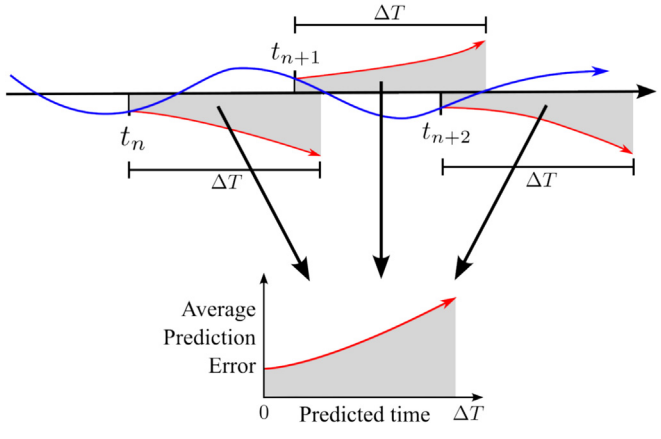

Fig. 2. The prediction performance evaluation combines all predicted trajectory arcs with a duration of ΔT over the evaluated time period to obtain an average prediction error.

The evaluation of the prediction process is done by comparing each individual arc against the reference orbit. This yields the prediction errors in the time interval $[t_n, t_n + \Delta T]$ shown as grey areas, where the error at t_n, i.e., the zero-age-of-data error matches the real-time orbit determination error. By evaluating the errors of all trajectory arcs over the full evaluation period, an average overall prediction error over the relative prediction time is obtained from the average of the individual absolute prediction errors.

3.4. Ephemeris fitting and user range error

In the context of LEO-PNT systems, the primary purpose of the predicted orbits consists in the generation of broadcast ephemerids parameters for the navigation message. In this context, the orbit prediction quality assessed in this study provides a lower bound for the overall error of the broadcast ephemerides. On top of the prediction error, the fit error of the utilized ephemeris model, i.e. the model's ability to represent the predicted trajectory, further contributes to the total error.

For a comparison of prediction and fit errors within the present study, a representative 20 parameter model is adopted, which has been previously been assessed and recommended by Meng et al. (2021b). The basic GNSS broadcast ephemeris model as used in, e.g., the GPS LNAV or Galileo I/NAV messages comprises a total of 15 parameters

$$\begin{aligned}&[a, e, i_0, di/dt, \Omega_0, \dot{\Omega}, \omega, M_0, \Delta n,\\ &\ C_{rc}, C_{rs}, C_{uc}, C_{us}, C_{ic}, C_{is}],\end{aligned} \tag{12}$$

including six Keplerian elements, i.e., semi-major axis a, eccentricity e, inclination i_0, longitude of the ascending node Ω_0, argument of perigee ω and mean anomaly M_0. These elements are extended by rates terms for inclination and ascending node with di/dt and $\dot{\Omega}$, respectively, as well as a mean motion difference Δn and sinusoidal correction terms C_x for the argument of latitude, the orbital radius, and the inclination. For LEO-PNT applications, the GNSS model is further augmented with additional trice-per-revolution harmonics and a rate term for the semi-major axis:

$$[C_{rc3}, C_{rs3}, C_{uc3}, C_{us3}, \dot{a}]. \tag{13}$$

Furthermore, to avoid singularities due to small eccentricity values, e and ω are substituted by (Xie et al., 2018)

$$\begin{aligned} e_x &= e \cdot \cos(\omega) \\ e_y &= e \cdot \sin(\omega) \end{aligned} \tag{14}$$

and a mean argument of latitude is introduced as

$$\lambda = M_0 + \omega. \tag{15}$$

The 20 parameters of the LEO-PNT ephemeris model are obtained in a least-squares adjustment, which uses a set of predicted position vectors as an input and then fits the ephemeris parameters to best match the given trajectory. In accord with the envisaged purpose of "real-time" broadcast ephemeris generation, the parameter adjustment is conducted over the previously selected prediction interval ΔT, which also defines the validity interval of the resulting ephemeris.

As a final performance metric for LEO-PNT, the orbit-only user ranging error (URE) is evaluated. It describes the projection of the LEO ephemeris errors on the line of sight and thus the contribution of these errors on the modeled pseudorange as experienced by a LEO-PNT user. It can be approximated by

$$\epsilon_{\mathrm{URE(orb)}} = \frac{\epsilon_{\mathrm{3DRMS(orb)}}}{\sqrt{3}} \tag{16}$$

where $\epsilon_{\mathrm{3DRMS(orb)}}$ is the 3D root mean square (RMS) error of the LEO broadcast ephemeris, i.e. the lumped errors of both fit and prediction with respect to the reference orbit.

4. Results and discussion

Based on the orbit determination and prediction methodology as well as the spacecraft data sets presented in the previous section, a performance evaluation for real-time orbit prediction of the four LEO satellites is carried out considering different cases of GPS-only or GPS/Galileo processing. First, the results of the real-time orbit determination are presented for a continuous 14d arc, which has been selected with focus on the current solar maximum and its implications on atmospheric drag in LEO. Thereafter, the real-time orbit prediction and ephemeris fitting process is assessed.

4.1. Real-time orbit determination

At each GNSS measurement epoch, the real-time navigation filter provides an updated estimate of the instantaneous position and velocity of the LEO satellite, which is subsequently used for orbit prediction. As a baseline, the filter uses only Galileo and GPS broadcast ephemerides, which are readily available on-board via the respective GNSS navigation signals. Furthermore, complementary results obtained with Galileo HAS corrections are presented alongside for performance comparison.

Fig. 3 shows the 3D orbit RMS error over the 14-day evaluation period for the four spacecraft. The results

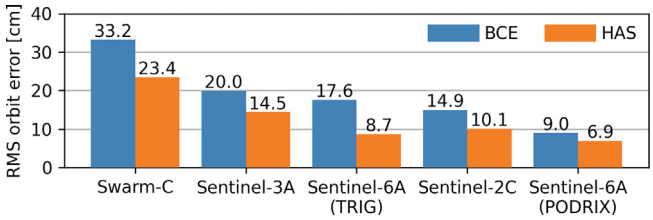

Fig. 3. 3D RMS error of real-time orbit determination over 14 days from DOY 333 to 346, 2024. Results obtained with broadcast ephemerides only are shown in blue, while Galileo HAS corrections were applied for the results depicted in orange. (For interpretation of the references to colour in this figure legend, the reader is referred to the web version of this article.)

clearly show the influence of both orbit altitude and Galileo processing. Swarm-C with GPS-only processing and a 460 km orbit shows the largest errors, while Sentinel-6A with Galileo/GPS measurements from the PODRIX receiver and an orbit height of 1336 km enables a sub-decimeter accuracy. The comparison between Sentinel-2C and Sentinel-3A at similar altitudes as well as between the two receivers on-board of Sentinel-6A shows the benefit of using Galileo measurements along with the superior quality of the Galileo broadcast ephemerides (Montenbruck et al., 2018). When using Galileo HAS corrections, the GPS-only scenarios exhibit the most significant performance improvement.

The high solar activity during the evaluation period causes and increased atmospheric density and atmospheric drag, which is most pronounced at lower altitudes. This effect is especially visible for Swarm-C at approximately 460km. In a previous study, a 3D orbit RMS error of 27.6 cm was obtained over 24h on DOY 259 in 2020 using broadcast ephemerides and a similar navigation filter (Hauschild and Montenbruck, 2021). When adopting the same filter settings with a value of $\sigma_{\mathrm{aemp,A}}$=15nm/s^2 and a correlation time $\tau = 600$s for DOY 2024/333 of the present evaluation period, a significantly larger 3D RMS error of around 60 cm is obtained. While the cross-track error remains similar, both radial and along-track axes exhibit a significantly larger error in 2024 compared to 2020. The Harris-Priester atmospheric density model employed in the real-time navigation filter assumes an average atmosphere at moderate solar activity. Close to a solar maximum, this model can no longer provide atmospheric density values with a sufficient accuracy. Consequently, the orbit determination performance significantly degrades in the along-track direction, where the atmospheric drag has its strongest impact. Due to the coupling of radial and along-track axes by means of the orbital dynamics, the radial axis also exhibits a larger error. Therefore, to account for the increased atmospheric density, a higher process noise of $\sigma_{\mathrm{aemp,A}}$=80nm/s^2 was adopted for Swarm-C in the 2024 analysis period. This reduces the 3D orbit RMS error to around 33 cm as shown in Fig. 3.

4.2. Real-time orbit prediction

Based on the orbit prediction algorithm and evaluation methodology described in Section 3, a real-time orbit prediction is carried out for all four spacecraft datasets. The GNSS measurement rate and thus the update rate of the real-time navigation filter is set to 30 s for all cases. As the ultimate goal of the prediction is to create a set of ephemeris parameters for a terrestrial or airborne LEO-PNT user, the overall prediction interval should ideally cover the duration of a satellite pass over a user. For the present study an interval of 20min is considered, which covers even the duration of a high elevation pass of Sentinel-6A. The prediction was performed with an integration step size of 30 s, i.e. a total of 40 consecutive DP5 steps are performed at each measurement interval to obtain a full 20 min predicted trajectory arc. As the navigation filter requires a certain convergence time, the first hour of the 14-day evaluation period is not used for prediction. Afterwards, the orbit prediction process is carried out every 5 min, resulting in approximately 4000 orbit arcs with a 20 min duration for each spacecraft.

Fig. 4 shows the average prediction error for all 20 min trajectory arcs over the evaluation period as solid lines, with the zero-age-of-data error representing the real-time orbit determination error. A distinction is made between GPS-only and Galileo/GPS cases in subfigures (a) and (b), respectively. Blue indicates the use of broadcast ephemeris only, while the results depicted in orange have been achieved using Galileo HAS corrections. In addition to the average prediction error, the error distributions are shown at 5-min steps in age-of-data as violin plots, with the dashed and dotted lines indicating median values as well as first and third quartiles.

Comparing these results once again shows the advantage of joint Galileo and GPS processing over the GPS-only test cases, when using only broadcast ephemerides for the modeling of GNSS orbits and clock offsets in the real-time navigation filter. Sentinel-3A (GPS-only) and Sentinel-2C (Galileo/GPS), which fly at similar altitudes, exhibit real-time orbit determination errors of 20 cm and 15 cm, respectively. On the other hand, the prediction error after 20 min grows to around 29 cm for both spacecraft,

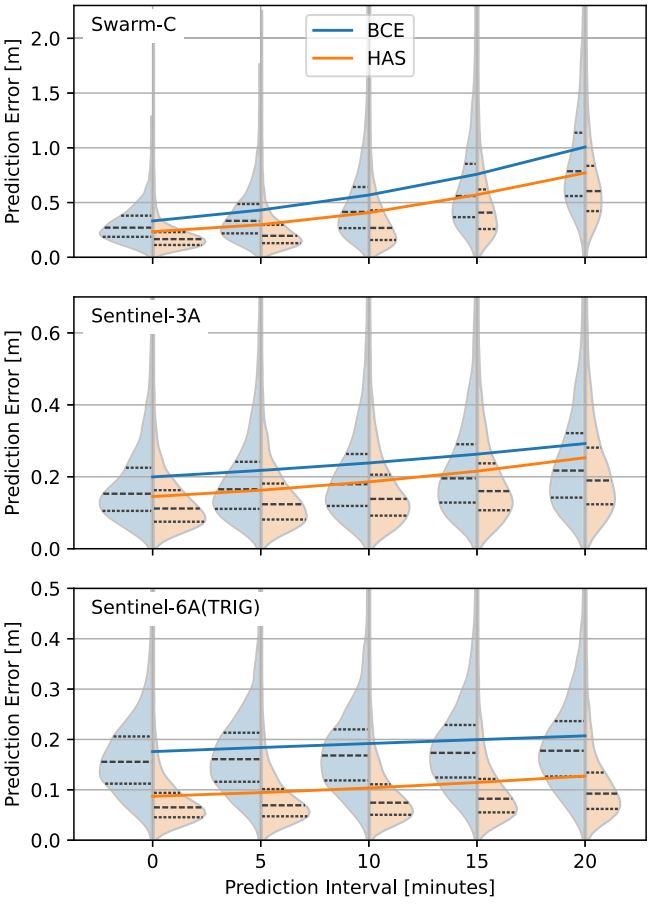

(a) GPS-only: Swarm-C, Sentinel-3A and Sentinel-6A (TriG receiver)

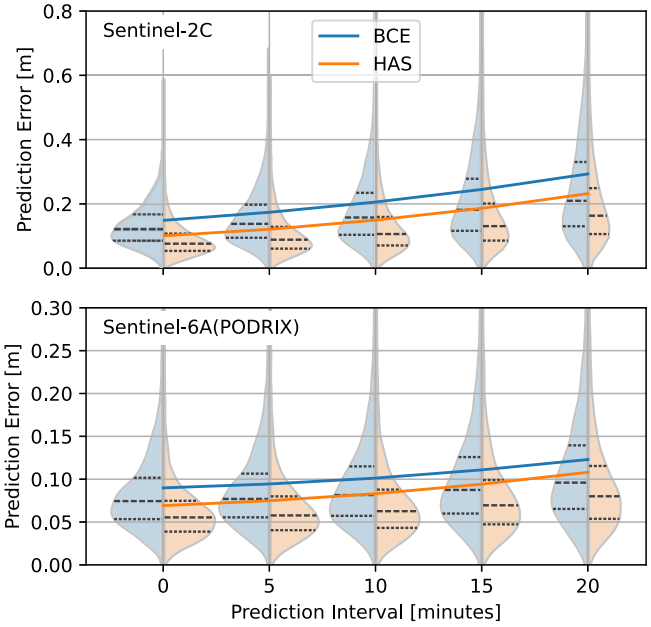

(b) Galileo/GPS: Sentinel-2C and Sentinel-6A (PODRIX receiver)

Fig. 4. Distribution of the 3D real-time orbit prediction errors as a function of the age-of-data, i.e. the time since start of prediction based on the real-time navigation solution, over 20 min with broadcast ephemerides (blue) and Galileo HAS corrections (orange). The solid lines indicate the average 3D RMS. Violin plots show the error distributions at discrete 5-min step in age-of-data, with the dashed and dotted lines indicating the median as well as 1st and 3rd quartiles. (For interpretation of the references to colour in this figure legend, the reader is referred to the web version of this article.)

which indicates a slightly degraded quality of the apriori drag modeling of Sentinel-2C as compared to Sentinel-3A. For Sentinel-6A, the performance of the Galileo/GPS solution obtained with the PODRIX data (9 cm 3D RMS real time position error and 12 cm error after 20 min prediction) is almost two times better than that obtained with TriG GPS-only data. As already seen in Section 4.1, Swarm-C exhibits the worst solution among all satellites considered here, which relates both to the limited SISRE of the GPS broadcast ephemerides and the increased atmospheric density at the fairly low orbital altitude. Overall, the average Swarm-C orbit prediction error increases to roughly 101 cm after 20 min.

Besides the results obtained with broadcast ephemerides only, Fig. 4 also shows the results using the Galileo High Accuracy Service. Using HAS enables a more accurate modeling of the measurements (c.f. Eqs. (10) and (11)) by applying additional orbit, clock and bias corrections, and thus improves the performance of the real-time orbit solution (Hauschild et al., 2022). The more precise satellite state vector estimate improves the initial conditions for the trajectory prediction and thus reduces the overall error of the propagated position and velocity in the prediction. Even though HAS corrections are not directly available for GPS-only receivers through the signal-in-space, the HAS corrections are most beneficial for a navigation system processing only GPS observations. With Swarm-C, the real-time and 20-min prediction errors are reduced from 33 cm to 23 cm and 101 cm to 77 cm, which amounts to an approximate 30 % improvement. In the case of Sentinel-6A TriG data processing, the results likewise improve by 50 % and 25 %, respectively. Sentinel-3A, however, exhibits a significantly smaller improvement, which can potentially be explained by the time-varying cross-section and a dominating impact of drag modeling errors irrespective of the GNSS ephemeris data quality.

For Sentinel-2C with Galileo and GPS observations, the overall orbit solution is improved by roughly 5 cm over the prediction interval, while for Sentinel-6A with multi-GNSS observations from the PODRIX receiver, the solution improves only marginally by less than 3 cm. However, with Galileo/GPS measurements from Sentinel-6A, the average orbit prediction error amounts to only around 12 cm after 20 min, significantly exceeding the performance of all other assessed spacecraft. Overall, the results using HAS corrections demonstrate an improvement for all spacecraft on both real-time and predicted orbit solutions. While the relative improvement is higher when working only with GPS data, the absolute performance of combined Galileo and GPS measurements using HAS is better, in general.

4.3. Considerations on prediction performance

4.3.1. Orbit altitude

While the quality of the GNSS ephemerides impacts the navigation solution through the measurement model independent of the satellite's orbit, the quality of the force model used in both the filter's time update and prediction routine is heavily dependent on the spacecraft altitude. With orbit perturbations becoming more complex to model at lower altitudes, mainly due to the increased influence of atmospheric drag and the asphericity of the gravitational potential, orbit determination using a reduced dynamic model becomes less accurate.

This is illustrated in Fig. 5, which evidences both an increased real-time orbit determination error as well as an increased relative growth of the prediction error over the forecast interval at low altitudes. Both aspects can best be observed in the comparison of Swarm-C and Sentinel-6A/TriG results. By way of example, the orbit error of Sentinel-6A at 1336 km altitude increases by only 20 % (9 cm to 12 cm) over the 20 min prediction interval, when using only broadcast ephemerides, while a threefold increase (33 cm to 101 cm) is encountered for Swarm-C at 460 km. The impact of the orbit altitude on the orbit determination and prediction performance is reduced when using Galileo HAS corrections, with the most significant impact on the results of Swarm-C.

The analysis clearly shows the benefit of orbital altitudes beyond 1000 km for the design of future LEO-PNT

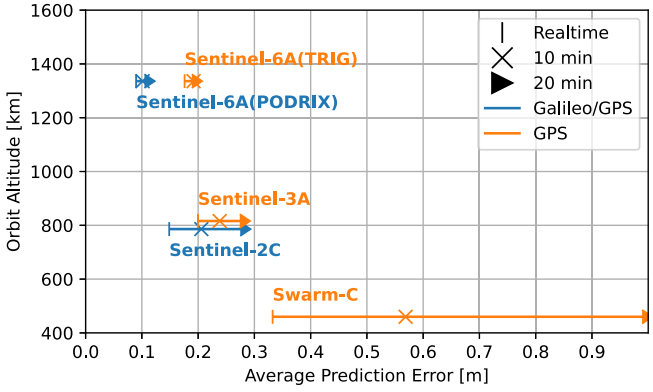

(a) Processing using BCE only

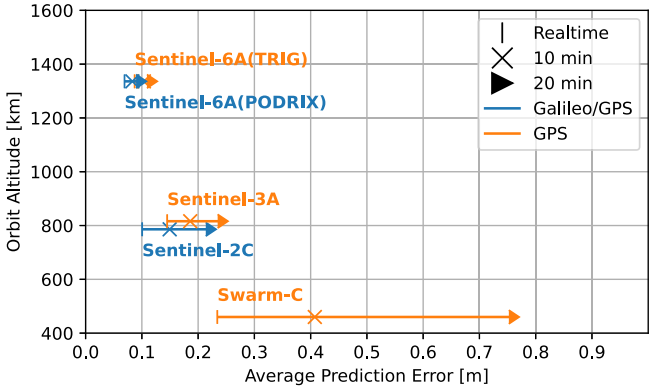

(b) Processing with HAS corrections

Fig. 5. Impact of altitude on the accuracy of real-time orbit determination solutions and orbit predictions of up to 20 min for the four different spacecraft using either GPS-only or Galileo/GPS measurements with broadcast ephemerides.

systems. In the absence of other mission constraints, the high altitude helps to minimize both real-time orbit determination and prediction errors and ultimately contributes to a favorable URE budget for LEO-PNT users. Furthermore, Fig. 5 once more shows the benefit of using Galileo on the overall navigation system performance due to the superior quality of its broadcast ephemerides. Both Sentinel-2C as well as Sentinel-6A/PODRIX results clearly outperform their respective GPS-only counterparts at similar altitudes, namely Sentinel-3A and Sentinel-6A/TriG, in terms of the achievable onboard orbit knowledge.

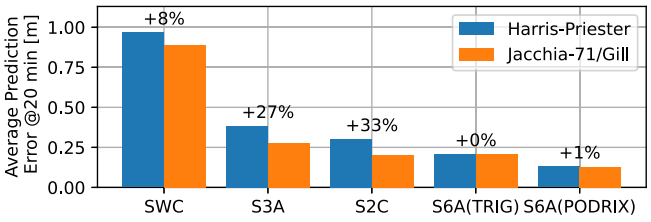

Fig. 6. Improvement of average 3D RMS error after 20 min prediction when using Jacchia-71/Gill instead of the Harris-Priester atmospheric density model.

4.3.2. Atmospheric density model

As already discussed in Section 4.1, the current solar maximum poses additional challenges on orbit determination using a reduced dynamic model at lower altitudes, with the 3D RMS error degrading significantly when using improper filter tuning or simplified atmospheric models. The example of Swarm-C demonstrated that the real-time orbit determination under these conditions can be significantly improved by increasing the process noise of the empirical acceleration in along-track. This approach in combination with the Harris-Priester model has been adopted as the default approach for this study. A different way to account for the increased atmospheric drag is to use a more elaborate atmospheric density model instead of altering process noise settings. For further illustration, the improvement of the average prediction error after 20 min for all spacecraft using Jacchia-71/Gill (Gill, 1996) instead of the Harris-Priester model is depicted in Fig. 6 for DOY 333 in 2024. For Swarm-C flying at the lowest altitude and thus experiencing the highest atmospheric drag, the prediction error with adapted process noise as discussed in Section 4.1 can be slightly improved by about 8 % from 97 cm to 88 cm. Sentinel-2C and Sentinel-3A on the other hand, despite orbiting significantly higher at around 800 km, benefit the most from the Jacchia-71/Gill model and show an improvement of approximately 30 % over use of the Harris-Priester model. This can be explained by their large area-to-mass ratios, which render the satellites more susceptible to atmospheric drag. For Sentinel-6A on the other hand, the model choice does not have any significant impact on the orbit solution, as atmospheric drag constitutes a negligible contribution to the overall perturbations.

In general, the benefit of a more complex atmospheric density model depends not only on the orbit altitude, but also on the satellite itself, including, for example, bus shape, surface properties, attitude variations and moving parts. The most significant downside of replacing the Harris-Priester model with a more complex model is the need for additional solar-geophysical parameters. In the case of Jacchia-71/Gill, these comprise both daily and averaged values of the solar radio flux ($F_{10.7}$ index), as well as the three-hourly geomagnetic K_p index. Those parameters would currently require frequent uploads to the LEO satellite via an uplink interface, thus creating an additional dependency on the ground segment that hampers a fully autonomous onboard operation. In the future, this problem can be solved with the introduction of the Galileo High Accuracy Service (HAS) Phase 2, where regular transmission of space weather parameters are foreseen (Galileo HAS SIS, 2023).

4.3.3. Navigation filter tuning

Since the navigation filter continuously provides the initial satellite state vector for the prediction process, the EKF tuning needs to be considered with the overall orbit determination and prediction process in mind. The previous results already identified the along-track axis error as the main contribution to the overall prediction error. This can be attributed to errors in the initial semi-major axis estimate as well as the impact of unmodeled perturbations during the prediction interval, both of which may induce secularly growing along-track errors. In the navigation filter, the along-track axis error can be influenced by tuning the process noise of the corresponding empirical acceleration as well as the drag coefficient C_D.

To demonstrate the impact of those variables on both the real-time and predicted orbit, a parametric study of the prediction performance was conducted for varying values of $\sigma_{\text{aemp,A}}$ or σ_{C_D}, and keeping otherwise identical navigation filter settings. Fig. 7 shows the 3D RMS of the real-time orbit determination and the average prediction error after 20 min as a function of the applied process noise for the example of Sentinel-3A with broadcast ephemerides on DOY 333. The left plot demonstrates the impact of $\sigma_{\text{aemp,A}}$ on the orbit solution, with the 20 min prediction exhibiting a significantly higher sensitivity than the real-time solution. For $\sigma_{\text{aemp,A}} = 10^{-8}\text{nm/s}^2$, the real-time solution and 20 min prediction have average errors of 27 cm and 45 cm, respectively. Increasing the process noise to $\sigma_{\text{aemp,A}} = 10^{-7}\text{nm/s}^2$ with otherwise identical filter settings increases the real-time error grows from about 11 cm to 38 cm, while the 20 min prediction error increases by almost 250 % to 1.11 m. While a moderate amount of process noise is indeed required to compensate force modeling errors and to obtain the best possible real-time navigation solution, excessive process noise reduces the length of the filter memory and its capability to accurately estimate the semi-major axis of the orbit (Carpenter and Schiesser, 2001). While this has only limited impact on the instanta-

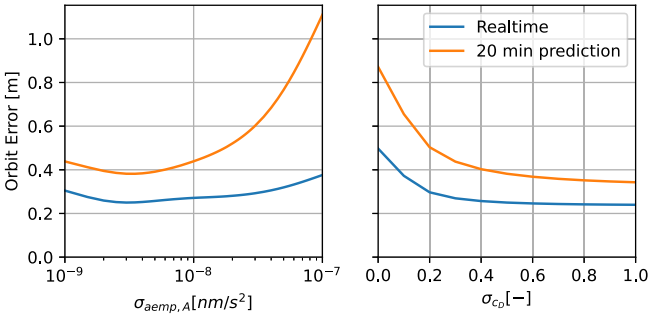

Fig. 7. Impact of process noise tuning for either empirical acceleration in along-track (left) or drag coefficient (right) on real-time and 20 min predicted orbit for Sentinel-3A.

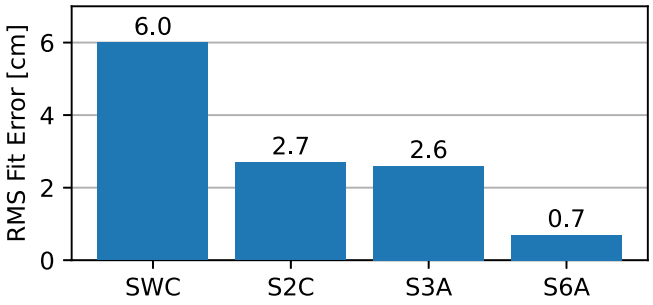

Fig. 8. Average RMS fit error over 14 days for all 20 min prediction arcs using the ephemeris model described in Section 3.4.

neous position error, it clearly degrades the prediction accuracy over extended fractions of the orbital revolution.

In general, the results in Fig. 7 demonstrate that careful tuning is required to optimize both real-time and predicted orbit solutions. Care must be taken, though, that the choice of optimal process noise values depends on the actual magnitude and variability of the air density and may need to be adapted over the duration of a mission in response to variations in solar and geomagnetic activity.

4.4. Comparison of prediction and fit errors

The results of the previous section demonstrate that representative error magnitudes between approximately 1 m (BCE)/ 70 cm (HAS) for Swarm-C at 460 km and 12 cm (BCE)/ 11 cm (HAS) for Sentinel-6A at 1336 km can be expected after a 20 min orbit prediction depending on the actual orbit altitude. However, for application on a LEO-PNT satellite, the predicted orbit also needs to be parameterized for transmission in a navigation message to users. To assess the impact of the ephemeris model adjustment on the overall error of the resulting LEO-PNT navigation message, we consider the 20-parameter model of Section 3.4 as an example and evaluate its fit error for the previously predicted trajectories. The position vectors used as input for this fit routine have an equidistant spacing of 30 s, which yields a total of 41 grid points over the 20 min fit interval and enables a sufficiently well-determined parameter adjustment. Fig. 8 depicts the average RMS fit error over all 20 min arcs. Similar to the previously shown prediction performance, the ephemeris model performance clearly depends on the spacecraft altitude, and exhibits a higher fit error at lower altitudes due to increased orbital perturbations at lower altitudes. Note that no distinction between BCE-only and HAS processing is made, as the fit error mainly depends on the orbit dynamics and is virtually the same in both cases. This also applies to the fit errors obtained from the results of the two GNSS receivers onboard of Sentinel-6A, which are also nearly identical. Due to the comparably small fit errors, the performance of the fitted ephemerides is, on average, only degraded by less than 6 % for all spacecraft when compared to the errors of the predicted trajectories themselves. This clearly shows that the major error source of LEO-PNT ephemerides generated in real-time is not the fitting but the prediction process.

As a final contribution to the performance assessment of LEO-PNT ephemerides, the total URE (Eq. (16)) including the joint contributions of prediction and fit errors is shown in Fig. 9. As the fit error has only a minor and rather uniform contribution over the 20 min, the URE shows essentially the same monotonic increase as the 3D prediction error presented previously in Section 4.2 and is again most pronounced at low altitudes. Likewise, the benefit of Galileo HAS corrections on the URE is most evident for the spacecraft with GPS-only measurements. Depending on the orbital altitude and the use GPS-only or GPS/Galileo processing in the real-time navigation system, UREs ranging from 60 cm (Swarm-C, BCE) down to 7 cm (Sentinel-6A, HAS) can be achieved over a 20 min forecast and fit interval.

5. Summary and conclusion

The study assesses the achievable performance of GNSS-based real-time orbit prediction on-board of a LEO satellite using a reduced dynamic orbit model and a real-time navigation filter. To ensure maximum onboard autonomy, only information obtainable via GNSS navigation messages were used, including broadcast ephemerides, optional Galileo HAS corrections and EOPs. In consideration of on-board ephemeris generation for LEO-PNT satellites, predicted trajectory arcs of 20 min were assessed. This duration covers the maximum visibility period of a LEO satellite as seen from Earth, allowing a potential LEO-PNT user to utilize the same set of ephemeris data during a single pass.

GNSS measurements of four LEO satellites across different orbit altitudes between 460 km and 1336 km were utilized for the assessment. For the real-time solution and predicted orbit arcs, a significant performance improvement is demonstrated when using combined Galileo and GPS over GPS-only observations, which can be attributed to the superior quality of the Galileo broadcast ephemerides. The orbit prediction can also be improved using

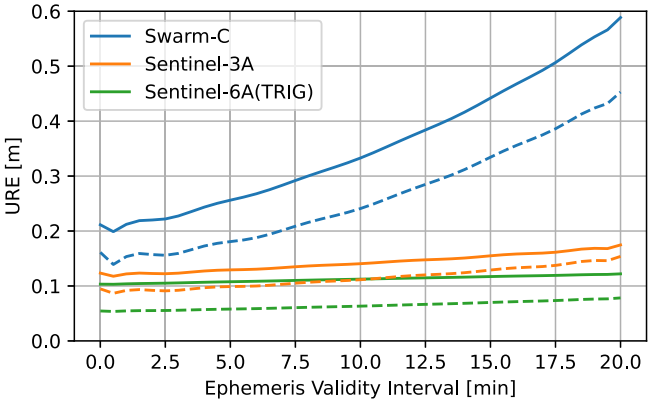

(a) GPS-only: Swarm-C, Sentinel-3A and Sentinel-6A (TriG receiver)

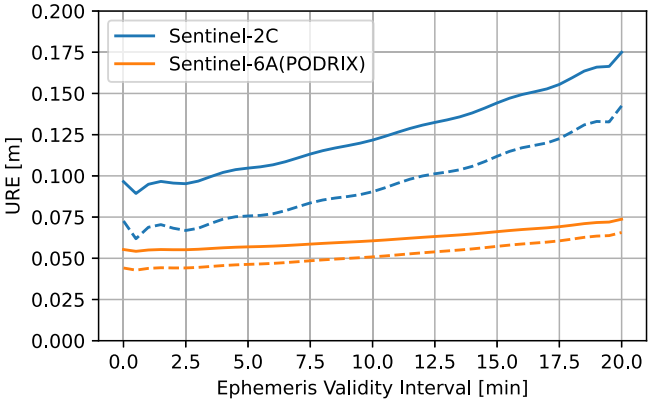

(b) Galileo/GPS: Sentinel-2C and Sentinel-6A (PODRIX receiver)

Fig. 9. User range error for the fitted ephemerides of the four spacecraft with GPS-only (a) and Galileo/GPS (b) measurements, averaged over the 14-day evaluation period. The ephemerides were generated based on the predicted trajectory arcs. Results obtained with broadcast ephemerides only as well as with HAS corrections are shown in solid and dashed lines, respectively.

Galileo HAS corrections in the real-time navigation filter, with a higher relative impact for GPS-only processing. Moreover, the significant dependence on altitude of the orbit determination and prediction performance could be demonstrated. At lower altitudes, satellites experience more pronounced orbit perturbations, which are harder to model especially in real-time. This consequently leads to an overall performance degradation at lower altitudes as shown by the example of Swarm-C. In view of the current solar maximum, it could be shown that coping with the increased atmospheric drag at lower altitudes poses a major challenge for both real-time orbit determination and prediction. To cope with this problem, the Jacchia-71/Gill atmospheric density model was tested over a 24 h period on DOY 333 as an alternative to the highly simplified Harris-Priester model. This approach improved the prediction performance after 20 min by up to 30 % for satellites at 800 km altitude, and suggests a benefit for the orbit prediction performance, which is subject to future research. However, additional parameters including $F_{10.7}$ and K_p indices are required for advanced density models. These are not currently available from GNSS navigation messages, but might be introduced in the upcoming Phase 2 of the Galileo High Accuracy Service. Furthermore, the impact of navigation filter tuning on real-time and predicted orbit solutions was assessed, with a focus on the process noise of the empirical acceleration in along-track direction as well as the drag coefficient. For both values, the prediction responds considerably more sensitive to the changes of those values, rendering a rigorous filter tuning mandatory to ensure best performance for both real-time and predicted solutions.

The sample case of Sentinel-6A processing with Galileo/GPS measurements and Galileo HAS corrections shows that real-time low Earth orbit predictions up to 20 min are possible with an average error of down to 11 cm even during solar maximum conditions, when orbiting at sufficiently high altitudes. Furthermore, it could be demonstrated that the main error source for LEO-PNT ephemerides generated in real-time remains the actual orbit prediction rather than the ephemeris model fit. The parametrization and adjustment of a representative extended Keplerian ephemeris model for LEO shows that the fit error of such a model is roughly one magnitude lower than the corresponding prediction error. In view of real-time onboard ephemeris generation for LEO-PNT, the orbit-only URE of the LEO ephemerides generated based on real-time orbit prediction was assessed. The study shows that an average URE of less than 7.5 cm over a validity interval of 20 min is possible when using multi-GNSS measurements on a high-altitude LEO satellite such as Sentinel-6A. In general, the results suggest that for LEO-PNT system with autonomous on-board ephemeris generation, high-altitudes orbits, availability of Galileo observations and ephemerides, and, optionally, usage of real-time correction services are the main factors for high URE performance, while the choice of a suitable LEO ephemeris model does not appear as a limiting factor.

Data availability

GNSS observations, attitude quaternions and auxiliary data for POD used in this study are publicly available at the Copernicus Data Space Ecosystem (https://dataspace.copernicus.eu/) and at the ESA Swarm Data Access platform (https://swarm-diss.eo.esa.int/) for the Sentinel and the SWARM-C spacecraft, respectively. GNSS broadcast ephemerides and precise orbit products are available from data centers of the International GNSS Service (IGS), including CDDIS (https://cddis.nasa.gov/archive/gnss/data/).

Declaration of competing interest

The authors declare that they have no known competing financial interests or personal relationships that could have appeared to influence the work reported in this paper.

Acknowledgments

The authors would like to thank the European Union (EU) and the Copernicus POD (CPOD) service for the provision of Sentinel spacecraft data, as well as the European Space Agency (ESA) and the Swarm project for the Swarm-C data used in this study. GNSS navigation messages used in this study were kindly provided by the IGS. The support of all station providers, analysis centers and data centers is gratefully acknowledged.

References

Carlin, L., Hauschild, A., Montenbruck, O., 2021. Precise point positioning with GPS and Galileo broadcast ephemerides. GPS Solutions 25 (2), 77. https://doi.org/10.1007/s10291-021-01111-4.

Carpenter, J.R., Schiesser, E.R., 2001. Semimajor axis knowledge and GPS orbit determination. Navigation 48 (1), 57–68. https://doi.org/10.1002/j.2161-4296.2001.tb00228.x.

Chen, L., Lv, F., Yang, Q., et al., 2023. Performance evaluation of CentiSpace navigation augmentation experiment satellites. Sensors 23 (12). https://doi.org/10.3390/s23125704.

Colombo, O., 1989. The dynamics of Global Positioning System orbits and the determination of precise ephemerides. J. Geophys. Res. Atmos. 94 (B7), 9167–9182. https://doi.org/10.1029/JB094iB07p09167.

Darugna, F., Casotto, S., Bardella, M., et al., 2022. Sentinel-6A GPS and Galileo dual-frequency real-time reduced-dynamics P2OD. In: 10th Workshop on Satellite Navigation Technology (NAVITEC). https://doi.org/10.1109/NAVITEC53682.2022.9847561.

De Oliveira Salgueiro, F., Cordero Limon, M., Giordano, P., 2024. A novel navigation message for LEO satellites. In: Proceedings of the 37th International Technical Meeting of the Satellite Division of The Institute of Navigation (ION GNSS+ 2024) (pp. 1082–1093). https://doi.org/10.33012/2024.19693.

Dobbin, M., Axelrad, P., 2023. A flexible ephemeris representation for GNSS and alternative PNT signal sources using b-splines. NAVIGATION: J. Inst. Navig. 70 (4). https://doi.org/10.33012/navi.610.

Donlon, C.J., Cullen, R., Giulicchi, L., et al., 2021. The Copernicus Sentinel-6 mission: Enhanced continuity of satellite sea level measurements from space. Remote Sens. Environ. 258, 112395. https://doi.org/10.1016/j.rse.2021.112395.

Dormand, J., Prince, P., 1980. A family of embedded Runge-Kutta formulae. J. Comput. Appl. Math. 6 (1), 19–26. https://doi.org/10.1016/0771-050X(80)90013-3.

Eissfeller, B., Pany, T., Dötterböck, D., et al., 2024. A comparative study of LEO-PNT systems and concepts. In: Proceedings of the ION 2024 Pacific PNT Meeting, pp. 758–782. https://doi.org/10.33012/2024.19646.

Fernández, J., Fernández, C., Féménias, P., et al., 2016. The Copernicus Sentinel-3 mission. In: ILRS workshop 2016, pp. 1–4.

Fernández, J., Peter, H., Fernández, C., et al., 2024. The Copernicus POD service. Adv. Space Res. 74 (6), 2615–2648. https://doi.org/10.1016/j.asr.2024.02.056.

Friis-Christensen, E., Lühr, H., Knudsen, D., et al., 2008. Swarm – an earth observation mission investigating geospace. Adv. Space Res. 41 (1), 210–216. https://doi.org/10.1016/j.asr.2006.10.008.

Galileo HAS SIS, 2023. Galileo High accuracy service E6-B signal-in-space message specification. https://ec.europa.eu/info/funding-tenders/opportunities/portal/screen/opportunities/tender-details/docs/b6d36029-040b-40c7-9699-2d743d2f6a9d-CN/Galileo-HAS-SIS-ICD-v2.0-(2022) 2776379_V1.pdf.

Gill, E., 1996. Smooth bi-polynominal interpolation of Jacchia 1971 atmospheric densities for efficient satellite drag computation, DLR-GSOC IB 96–1. DLR-GSOC IB 96-1, DLR Oberpfaffenhofen.

Gini, F., 2024. RINEX - The Receiver Independent Exchange format version 4.02. https://files.igs.org/pub/data/format/rinex_4.02.pdf.

GPS ICD, 2022. NAVSTAR GPS Space Segment/Navigation User Segment Interfaces, IS-GPS-200, rev. N, 22 Aug. 2022, Space Systems Command (SSC). https://www.gps.gov/technical/icwg/IS-GPS-200N.pdf.

Gunning, K., Blanch, J., Walter, T., 2019. SBAS corrections for PPP integrity with solution separation. In: Proceedings of the 2019 International Technical Meeting of the Institute of Navigation, pp. 707–719. https://doi.org/10.33012/2019.16739.

Guo, X., Wang, L., Fu, W., et al., 2022. An optimal design of the broadcast ephemeris for LEO navigation augmentation systems. Geospatial Inform. Sci. 25 (1), 34–46. https://doi.org/10.1080/10095020.2021.2017760.

Hairer, E., Wanner, G., Nørsett, S.P., 1987. Solving Ordinary Differential Equations I. Springer-Verlag, Berlin-Heidelberg-New York.

Harris, I., Priester, W., 1962. Time-dependent structure of the upper atmosphere, NASA TN-1443. Goddard Space Flight Center, MD.

Hauschild, A., Montenbruck, O., 2021. Precise real-time navigation of LEO satellites using GNSS broadcast ephemerides. NAVIGATION, J. Inst. Navigat. 68 (2), 419–432. https://doi.org/10.1002/navi.416.

Hauschild, A., Montenbruck, O., Steigenberger, P., et al., 2022. Orbit determination of Sentinel-6A using the Galileo high accuracy service test signal. Gps Solutions 26 (4), 120. https://doi.org/10.1007/s10291-022-01312-5.

Iannucci, P.A., Humphreys, T.E., 2022. Fused Low-Earth-Orbit GNSS. https://doi.org/10.1109/TAES.2022.3180000. arXiv:2009.12334.

Jacchia, L.G., 1971. Revised static models of the thermosphere and exosphere with empirical temperature profiles. SAO Special Report# 332 (1971), 332.

Kozhaya, S., Saroufim, J., Kassas, Z.Z.M., 2025. Unveiling Starlink for PNT. NAVIGATION: J. Inst. Navigat. 72 (1). https://doi.org/10.33012/navi.685.

Kunzi, F., Braun, B., Markgraf, M. et al., 2023. A GNSS-synchronized satellite navigation payload for LEO PNT. In: Proceedings of the 36th International Technical Meeting of the Satellite Division of The Institute of Navigation (ION GNSS+ 2023) (pp. 1425–1435). https://doi.org/10.33012/2023.19322.

Le Priellec, A., Giordano, P., Cordero Limon, M. et al., 2025. LEO-PNT end-to-end in-orbit demonstration: an ESA initiative to pave the way for a European GNSS constellation in LEO. In: M. Petrozzi-Ilstad (Ed.), Small Satellites Systems and Services Symposium (4S 2024) (p. 1354633). International Society for Optics and Photonics SPIE volume 13546. https://doi.org/10.1117/12.3062635.

McCarthy, D.D., 1996. IERS Conventions (1996). IERS Technical Note 21, US Naval Observatory. https://ilrs.gsfc.nasa.gov/docs/1996/iers_1996_conventions.pdf.

Meng, L., Chen, J., Wang, J., et al., 2021a. A broadcast ephemeris design of LEO navigation augmentation satellites based on the integration-type ephemeris model. Meas. Sci. Technol. 32 (8), 085009. https://doi.org/10.1088/1361-6501/abfaf5.

Meng, L., Chen, J., Wang, J., et al., 2021b. Broadcast ephemerides for LEO augmentation satellites based on nonsingular elements. GPS Solutions 25 (4), 129. https://doi.org/10.1007/s10291-021-01162-7.

Montenbruck, O., Gill, E., 2000. Satellite Orbits: Models, Methods, and Applications. Springer, Berlin, Heidelberg.

Montenbruck, O., Gill, E., 2001. State interpolation for on-board navigation systems. Aerosp. Sci. Technol. 5 (3), 209–220. https://doi.org/10.1016/S1270-9638(01)01096-3.

Montenbruck, O., Hauschild, A., 2013. Code biases in multi-GNSS point positioning. In: Proceedings of the 2013 International Technical Meeting of The Institute of Navigation, pp. 616–628.

Montenbruck, O., Kunzi, F., Hauschild, A., 2022. Performance assessment of GNSS-based real-time navigation for the Sentinel-6 spacecraft. GPS Solutions 26 (1), 12. https://doi.org/10.1007/s10291-021-01198-9.

Montenbruck, O., Ramos-Bosch, P., 2008. Precision real-time navigation of LEO satellites using global positioning system measurements. GPS Solutions 12 (3), 187–198. https://doi.org/10.1007/s10291-007-0080-x.

Montenbruck, O., Steigenberger, P., Hauschild, A., 2018. Multi-GNSS signal-in-space range error assessment – methodology and results. Adv. Space Res. 61 (12), 3020–3038. https://doi.org/10.1016/j.asr.2018.03.041.

Peter, H., Springer, T., Zangerl, F. et al., 2022. Beyond gravity PODRIX GNSS receiver on Sentinel-6 Michael Freilich–receiver performance and POD analysis. In: Proceedings of the 35th International Technical Meeting of the Satellite Division of The Institute of Navigation (ION GNSS+ 2022), pp. 589–601. https://doi.org/10.33012/2022.18368.

Reid, T., Banville, S., Chan, B. et al., 2022. PULSAR: A new generation of commercial satellite navigation. ION GNSS+ 2022, pp. 11–15.

Rizos, C., Stolz, A., 1985. Force modelling for GPS satellite orbits. In: Proc. 1st Int. Sym. Precise Positioning with GPS, Rockville, MD (pp. 87–98). Volume 1.

Schutz, B., Tapley, B., Born, G.H., 2004. Statistical orbit determination. Elsevier.

Steigenberger, P., Montenbruck, O., Bradke, M., et al., 2022. Evaluation of earth rotation parameters from modernized GNSS navigation messages. GPS Solutions 26 (2), 50. https://doi.org/10.1007/s10291-022-01232-4.

Tapley, B.D., Bettadpur, S., Watkins, M., et al., 2004. The gravity recovery and climate experiment: mission overview and early results. Geophys. Res. Lett. 31 (9). https://doi.org/10.1029/2004GL019920.

Tetewsky, A., Ross, J., Soltz, A. et al., 2009. Making Sense of Inter-Signal Corrections - Accounting for GPS Satellite Calibration Parameters in Legacy and Modernized Ionosphere Correction Algorithms. InsideGNSS, (pp. 37–48a).

van den IJssel, J., Encarnação, J., Doornbos, E. et al., 2015. Precise science orbits for the Swarm satellite constellation. Adv. Space Res., 56 (6), 1042–1055. https://doi.org/10.1016/j.asr.2015.06.002.

Van Uytsel, W., Janssen, T., Weyn, M., et al., 2024. A technical overview of current "New Space" LEO-PNT initiatives and their application potential. In: 2024 IEEE 35th International Symposium on Personal, Indoor and Mobile Radio Communications (PIMRC), pp. 1–6. https://doi.org/10.1109/PIMRC59610.2024.10817274.

Wang, F., Gong, X., Sang, J., et al., 2015. A novel method for precise onboard real-time orbit determination with a standalone GPS receiver. Sensors 15 (12), 30403–30418. https://doi.org/10.3390/s151229805.

Wu, S.-C., Yunck, T.P., Thornton, C.L., 1991. Reduced-dynamic technique for precise orbit determination of low Earth satellites. J. Guid., Control, Dynam. 14 (1), 24–30. https://doi.org/10.2514/3.20600.

Xie, X., Geng, T., Zhao, Q., et al., 2018. Design and validation of broadcast ephemeris for low Earth orbit satellites. GPS solutions 22 (2), 54. https://doi.org/10.1007/s10291-018-0719-9.

Young, L., 2017. JPL GNSS receivers, past, present, and future. In: SCaN/HEOMD Workshop on Emerging Technologies for Autonomous Space Navigation. https://api.semanticscholar.org/CorpusID:217251015.